Terahertz spectroscopy from air plasmas created by two-color femtosecond laser pulses: The ALTESSE project

L. Bergé, K. J Kaltenecker, S. Engelbrecht, A Nguyen, Stefan Skupin, L Merlat, B Fischer, B. Zhou, I. Thiele, P. U Jepsen

Terahertz spectroscopy from air plasmas created by two-color femtosecond laser pulses: The ALTESSE project

L. Bergé[1], K. Kaltenecker[2], S. Engelbrecht[3], A. Nguyen[1], S. Skupin[4], L. Merlat[3], B. Fischer[3], B. Zhou[2], I. Thiele[5] and P. U. Jepsen[2]

[1] *CEA, DAM, DIF - 91297 Arpajon - France*
[2] *DTU Fotonik - Dept. Photonics Engineering, Technical University of Denmark, DK-2800 Kongens Lyngby, Denmark*
[3] *Institut franco-allemand de recherches de Saint-Louis, 5 rue du Général Cassagnou, 68300 Saint-Louis - France*
[4] *Institut Lumière Matière, UMR 5306 Université Lyon 1 - CNRS, Université de Lyon, 69622 Villeurbanne, France*
[5] *Department of Physics, University of Gothenburg, SE-412 96 Göteborg, Sweden*

PACS 42.65.Re – Ultrafast processes; optical pulse generation and pulse compression
PACS 32.80.Fb – Photoionization of atoms and ions
PACS 52.38.-r – Laser-plasma interactions

Abstract –Terahertz pulses are very popular because of their numerous applications, for example in security. Located between microwaves and optical waves in the electromagnetic spectrum, their spectral domain can now be exploited for molecular spectroscopy using terahertz emission from plasmas formed by femtosecond laser pulses ionizing gases such as air. Downconversion of broadband optical spectra in a plasma produces intense radiation suitable for the detection of suspect materials remotely. The different physical mechanisms involved to create terahertz radiation by laser-material interaction are reviewed. The new potentialities offered by intense lasers allow the acquisition of unique spectral signatures characterizing various materials.

Introduction. – Until the nineties, the domain of terahertz waves (THz), which extends between 100 GHz and a few tens of THz in the electromagnetic spectrum (fig. 1), was barely explored. This situation radically changed 30 years ago with the advent of the THz time domain spectroscopy (TDS) and its impact in all sectors of science [1]. Terahertz spectroscopy has indeed become an important tool for studying molecules in the condensed phase. In particular, many chemical, biological, radiological, nuclear and explosive agents that represent warfare hazards exhibit characteristic spectral features in this frequency region, which has thus a strong potential for security applications [2–9]. Various materials such as paper, leather, cotton and synthetic fabrics are transparent in the THz frequency range, which is one of its main advantages for scanning purposes. THz photons only excite free carriers, optical phonons, vibrations and molecular rotations. They have a relatively weak energy and the available THz-TDS systems deliver low radiation power (< 1 mW), so that they do not pose a health risk [11]. Besides homeland security, THz-TDS offers a wide range of applications (see fig. 2). For instance, in medical imaging, THz radiation provides good contrasts for detecting certain cancers [12].

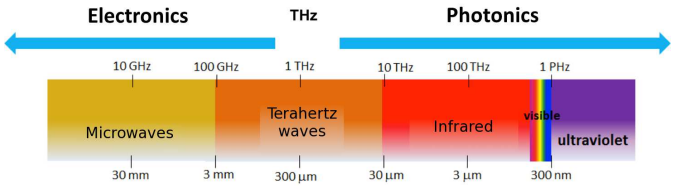

Fig. 1: Terahertz domain in the electromagnetic spectrum.

It can also be used for the detection of greenhouse gases and monitoring of flora [13]. However, because water is opaque to THz waves, the current challenge in atmospheric THz technology is to overcome the high absorption of ambient humidity, which can extinguish the THz radiation over 1-m-long distances. There is thus a growing demand for intense THz sources. An important requirement in spectroscopy is also to cover large spectral bandwidths, in order to collect as many molecular signatures as possible.

This Perspective article mainly focuses on THz spectroscopy applications employing laser-based coherent sources and detection techniques. After a review of laser-driven THz devices and their underlying physics, empha-

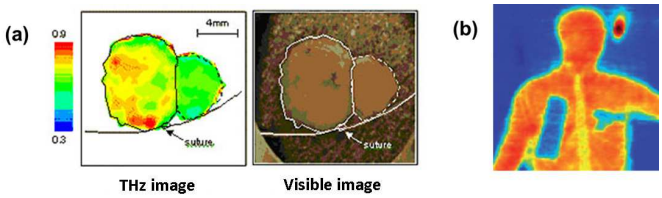

Fig. 2: (a) Terahertz imaging revealing epithelial cancer (red areas), not detected in visible imaging (source: http://www.teraview.com). (b) THz image of an individual concealing suspicious objects under his clothes (Photo Arttu Luukanen, Millilab, Espoo, Finland).

sis is given to recent results obtained in the framework of the French project ALTESSE devoted to the THz spectroscopy of powders, including explosives.

Terahertz transmitters and detectors: from electronics to lasers. – THz sources can be divided into three categories [1, 14, 15]: Solid-state electronic devices, quantum-cascade lasers (QCLs) and optically-induced THz emitters. Electronic devices, e.g., Schottky diodes [16, 17], usually emit weak and narrowband (< 3 THz) radiation. QCLs are unipolar devices where lasing is achieved through intersubband transitions in stacks of semiconductor quantum-well heterostructures [18,19]. Although they are frequency-tunable, their emitted pulses, however, remain still narrowband within a few THz [20, 21]. Therefore, only sources of the last category are of significant relevance for THz-TDS.

Optically-based THz emitters. The first optically-induced emitters are photoconductive switches (PCS) that consist of semiconductors equipped with a pair of electrodes between which a high voltage is applied. A femtosecond laser pulse creates electron-hole pairs in the semiconductor, producing a current flow between the electrodes. Since the current is changing typically over one picosecond, the electrodes act as THz-emitting antennas [22]. In general, THz amplitudes cannot excess the MV/m level and the energy yield saturates with the laser pulse energy [23]. THz radiation broadened to 20-30 THz has been demonstrated by using low-temperature grown GaAs or semi-insulating GaAs with ultrashort pulses [24, 25]. Laser-to-THz conversion efficiency up to $\sim 2 \times 10^{-2}$ can be achieved [26], e.g., by means of plasmonic electrodes, and quasi-single-cycle THz waveforms with 10 μJ energy, 33 MV/m THz field strength have been generated from ZnSe interdigited PCSs [27].

Other THz transmitters proceed from optical rectification (OR) in nonlinear crystals [28]. Non-centrosymmetric crystals exhibit a $\chi^{(2)}$-nonlinearity, proportional to the square of the exciting laser field. Besides frequency doubling, this nonlinearity leads to down-conversion towards the THz range. Here, two-photon absorption and pump depletion limits the THz yield [29], together with the phase mismatch between the optical group velocity and the phase velocity of the THz wave. ZnTe crystals [30] can radiate below 3 THz and offer conversion efficiency around 3×10^{-5} [30, 31]. As an alternative, $LiNbO_3$ crystals have low THz absorption, higher nonlinear coefficients and higher damage threshold. However, their linear dispersion is strong. Phase-matching conditions can then be optimized by introducing a tilt angle in the pulse front with a diffraction grating [32, 33]. Typical tilted-pulse-front LiNbO3 THz sources (abbreviated TPF in Table 1 below) provide peak electric fields > 20 MV/m in the spectral window ≤ 4 THz, with high conversion efficiencies $\geq 10^{-2}$ and $> 15\,\mu$J energies [32, 34, 35]. An attractive alternative is the organic crystal DSTMS characterized by nonlinear coefficients one order of magnitude larger than $LiNbO_3$ and good phase-matching. With DSTMS, THz electric fields of ~ 0.4 GV/m have been generated [36].

The emitters discussed so far supply a very limited bandwidth of a few THz. Gas-plasma THz emitters overcome this limitation by offering bandwidths exceeding 40 THz. Two decades ago, THz pulses produced at moderate laser intensities $\sim 10^{14}$ W/cm^2 were created from single-color pulses ionizing air under an external strong bias field [37]. A combination of two colors was rapidly proposed, resulting in an increase of the THz energy by a factor 40 [38, 39]. Early works on this technique reported peak THz fields of 15 MV/m, bandwidths as broad as 75 THz [40, 41] and $\sim 10^{-4}$ conversion efficiencies. The standard two-color scheme focuses a fundamental (FH) laser pulse onto a β-barium-borate (BBO) crystal placed before the focus of a converging lens. The BBO crystal creates the second harmonic (SH) field and both harmonics co-propagate towards a common focal spot. In air the resulting two-color laser pulse ionizes O_2 and N_2 molecules at atmospheric pressure close to focus. This creates an electron plasma, called "air plasma", that produces a macroscopic current leading to broadband THz emission.

This technique has several advantages over conventional THz sources: First, fs-broadband laser pulses generate extended THz spectra. Second, high amplitude THz fields close to the GV/m level can be produced without any risk of damaging the source. Third, the regime of laser filamentation, reached through a local balance between Kerr self-focusing and plasma generation [42, 43], makes it possible to generate THz pulses remotely in the atmosphere [44–46], and thus bypass the absorption of THz frequencies by water molecules. Fourth, the energy contained in the THz pulse can strongly increase with several laser parameters, including the fundamental pump wavelength [47], the laser pulse duration [48] and the number of colors composing the pump pulse [49].

Last but not least, laser pulses with ultra-high intensities $> 10^{18}$ W/cm^2 can also produce energetic THz waves in relativistic interaction regimes [50]. The advantages of such THz pulses are manyfold: They are highly energetic, close to the mJ level [51], and broadband with about 70% of the THz energy located in the region < 10 THz [52, 53]. Among the main mechanisms generating

Table 1: Performances of various methods for generating intense THz waves [58]. THz fields are expressed in GV/m; frequencies and bandwidth are expressed in THz. CE = conversion efficiency; CF = Central frequency; BW = Bandwidth.

Method	THz field	CE	CF	BW
PCS	< 0.1	10^{-4}	~ 2	~ 5
2C	0.8	10^{-3}	$\sim 5-10$	> 50
OR	8.3	10^{-2}	$\sim 1-4$	~ 5
TPF	0.1	10^{-3}	~ 0.8	~ 2
UHI	> 10	5×10^{-4}	$1-10$	≥ 10

THz pulses we find linear mode conversion [52], transient currents at the target rear surface [53] and coherent transition radiation excited when accelerated electrons go across a plasma/vacuum interface with relativistic velocities [54–56]. THz emissions from thin Ti foils was recently measured with ~ 0.7 mJ THz energies, field strengths of ~ 10 GV/m and 10-THz bandwidth [57].

Table 1 summarizes the most recent performances (see also [58]) reported from the above technologies.

Detection of intense THz waveforms and spectra. There are several ways to detect THz radiation coherently.

The most common technique relies on the ultrafast Pockels effect, where THz radiation is collected by an electro-optical crystal, for example ZnTe [59,60]. The THz field induces an instantaneous birefringence in the electro-optic medium, which is probed with a second laser pulse split from the pump source. To obtain the THz electric field in time domain, the signal is recorded as a function of the time delay between the THz and probe pulse. For measuring broadband, intense THz pulses, temporal walk-off due to velocity mismatch, however, puts severe conditions on the crystal thickness. This method may also introduce ambiguities linked to phase jumps [61].

Detection by air nonlinearities is possible as well [62–65]. Here, the THz beam is recombined with the fundamental at a second focus forming the detection region where an electric bias field is applied. This technique is called "ABCD" (Air-Biased Coherent Detection) [66]. A sketch of the ABCD scheme is shown in fig. 5 commented later. A plasma created by a two-color pulse emits THz radiation towards a sample. This radiation is filtered and directed to the detection part. Here, a probe pulse with controlled delay is focused between two electrodes where an alternating field of 20 kV/cm is applied. The nonlinear response of air produces second harmonic of the probe pulse that overlaps with the THz field of interest. The interaction of the fundamental laser field E_ω and the low frequency field components can thus be described by $E_{2\omega} \propto \chi^{(3)} E_\omega E_\omega E_{\mathrm{THz}}$, where $\chi^{(3)}$ denotes the third-order susceptibility of air. So, the second harmonic intensity, which is the measured quantity, is proportional to the THz wave intensity. To get coherent detection, the AC bias voltage is synchronized at half the laser repetition rate.

Another detection technique is the spectral-domain interferometry (SDI), recently extended for THz field measurements [61, 67]. Conventional SDI employs a broadband light source to illuminate a reference surface and a sample, recombined in a Michelson interferometer [14]. In the SDI THz variant, two optical probe pulses with a certain delay are focused into a ZnTe crystal, overlapping with the THz pulse to be measured. The delay is chosen such that the birefringence induced by the THz pulse via Pockels effect is experienced by the second pulse only. Then, the two probe pulses are sent into a spectrometer and the THz pulse is retrieved from interference between the two pulses. Alternatively, THz waves can also be detected indirectly by THz Radiation Enhanced Emission of Fluorescence (THz-REEF) that amounts to extracting spectral information on the THz pulse from the plasma fluorescence [68–70]. Using two color filaments, Liu and co-workers performed a THz remote sensing at a distance of 10 m [69]. To end with, let us mention the potential use of solid dielectrics to exploit their strong $\chi^{(3)}$ coefficient. A recent study demonstrated the first solid-state scheme for THz coherent detection relying on electric-field-induced SH generation by a thin layer of fused silica [71].

Main physical mechanisms. – An ultrashort optical pulse can be converted into the THz range via specific nonlinearities, namely, (i) the Kerr effect, (ii) photoionization and (iii) plasma waves associated to ponderomotive forces. The relevance of these mechanisms depends on the intensity level engaged, as summarized in fig. 3.

Four-wave mixing. This mechanism was proposed to interpret the first experiments using two-color laser pulses in air [38]. The polarization vector of the medium contains nonlinear contributions that express in cubic power of the electric field (Kerr effect), namely, $P_{\mathrm{NL}} = \epsilon_0 \chi^{(3)} E_L^3$. This nonlinearity mixes the two harmonics, resulting in the production of low frequencies. Ignoring spatial dependencies, a two-color laser field can be modelled as

$$E_L(t) = \sqrt{\frac{2I_0}{c\varepsilon_0}} \sum_{j=1,2} a_j \, \mathrm{e}^{-2\ln 2 \frac{t^2}{\tau_j^2}} \cos(j\omega_0 t + \varphi_j), \qquad (1)$$

where I_0 is the pump intensity, τ_j is the FWHM duration of the jth harmonic ($j = 1, 2$), $r = a_2^2/a_1^2$ is the SH/FH intensity ratio with $a_1^2 + a_2^1 = 1$, and $\varphi = \varphi_2 - \varphi_1$ is the relative phase between the two carrier waves. In the plane wave approximation ($\tau_j \to +\infty$), the Kerr nonlinearity produces a quasi-static component $P_{\mathrm{NL}}^{\mathrm{dc}} \propto a_1^2 a_2 \cos\varphi$ assimilated to a THz emitter and maximum for in-phase laser harmonics ($\varphi = 0$). Four-wave mixing is, however, too weak to explain the observed THz field strengths [39]. Recent experiments [72] showed that its signature is actually present in the THz spectrum for intensities less than the ionization threshold of air molecules $\sim 5 \times 10^{13}$ W/cm^2. Nevertheless, Kerr contributions, including the effect of delayed Raman scattering, are usually two to

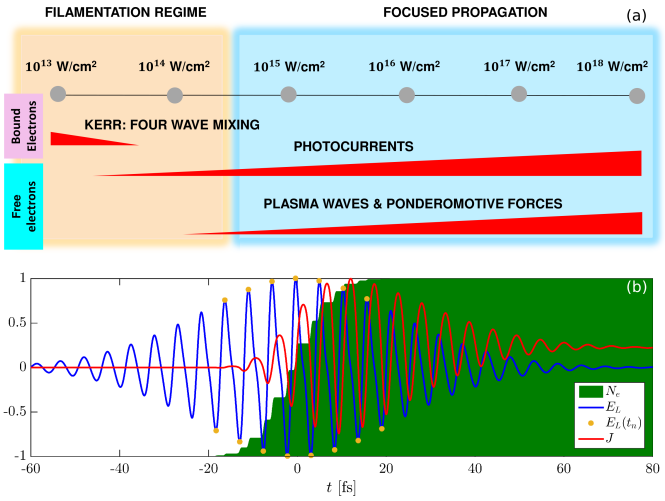

Fig. 3: (a) Mechanisms generating THz waves by intense two-color laser pulses, distributed according to the optical intensity. The first region involves the Kerr effect (four-wave mixing) and photoionization. The second region accentuates the contribution of photoionization in the tunnel regime (photocurrents) and involves plasma waves created by ponderomotive forces. (b) Photocurrent process: The two-color electric field generates free electrons in stepwise increase via tunneling ionization occurring near the field extrema at $t = t_n$. This builds a slow component of the current that acts as a THz source.

three orders of magnitude lower compared to those coming from photocurrents [74].

The photocurrents. In 2008, Kim et al. [40] understood that generating a current of free electrons by photoionization is the key process dominating THz wave generation by two-color laser pulses. The so-called "local current" (LC) model, worked on by Babushkin *et al.* [73], allowed to explain how this terahertz radiation is produced from "photocurrents". This model assumes that the radiated electric field is proportional to the time derivative of the electron current, i.e., $E_{\rm THz} \propto \partial_t J$. At intensities larger than 10^{13} W/cm^2, ionization takes place in the tunneling regime [75]. The strength of the laser electric field is high enough to lower the Coulomb potential of the atom, so that the electrons can tunnel out of the potential barrier. Ionization occurs near the extrema of $E_L(t)$ located at times t_n. The density of free electrons, N_e, rises from the gas density N_a with the ionization rate $W(t)$ [77] as

$$\partial_t N_e = W(t)(N_a - N_e), \tag{2}$$

and it increases by successive steps δN_n as $N_e(t) \simeq \sum_n \delta N_n H_n(t-t_n)$, where the function $H_n(t-t_n)$ is close to the Heaviside step function [73].

For a linearly-polarized laser pulse the current density can be expressed in scalar form:

$$(\partial_t + \nu_c)J = \frac{e^2}{m_e} N_e E, \tag{3}$$

where ν_c is the electron collision rate equal to a few ps^{-1}. Given the previous approximation on $N_e(t)$, the current $J(t)$ can be divided into two distinct contributions, $J(t) \simeq J_A(t) + J_B(t)$ [73, 74]. $J_A(t)$ is the fast current component that mainly describes generation of harmonics due to photoionization. $J_B(t)$ depends on the product $\sum_n \delta N_n v_f(t_n)$, where $v_f(t_n)$ denotes the electron velocity at instant t_n, and contains a low frequency component responsible for THz emission.

Figure 3(b) summarizes THz generation by a two-color pulse. Ionization appears near the extrema of the laser electric field, inducing peaks in the rate $W(t)$ from which N_e increases steplike. Asymmetry in the two-color pulse profile guarantees non-zero velocities $v_f(t_n) \propto \sin\varphi$. The low frequency component in $J_B(t)$ is maximum for relative phases of $\pi/2$ between the two colors. This model has been validated by experiments and 3D simulations [78]. A single-color laser field generates almost no THz radiation. With two colors, two orders of magnitude can be gained in the THz energy yield as $\varphi \to \pi/2$ [79]. The LC model shows that THz fields can be enhanced by a judicious arrangement of the laser harmonics. A sawtooth profile can achieve in theory the record conversion rate of 2% [49]. THz pulse generation with uncommon frequency ratios of 1:4 and 2:3 has also been experimentally tested [80]. In space, THz emission takes place along small angles determined by phase-matching conditions and changes in the refraction index due to plasma, depending on the length of the plasma channel [81].

Plasma wakefields. When the laser pump delivers higher intensities $> 10^{15}$ W/cm^2, other nonlinear mechanisms can act as frequency converter. This is the case of plasma waves, for which Eq. (3) must be supplemented by the Lorentz force and quadratic terms in J associated to ponderomotive motions [82, 83]. Once ionized, the free electrons are dragged by the laser field out of their equilibrium position via the Lorentz force. This displacement of charges forces the electrons to oscillate around ions in the wake of the laser pulse at the electronic plasma frequency $\omega_{\rm pe} = e^2 N_e/\epsilon_0 m_e$ (ϵ_0 is the vacuum permittivity). This frequency takes typical values between 20 and 60 THz for densities between 10^{17} and 10^{18} cm^{-3}. However, it is not guaranteed that, outside the created plasma, such fields can be transmitted to a detector [84, 85]. This depends on the plasma volume and geometry (e.g., the gradients), the emissivity of which can also be controlled by playing with the transverse laser polarization [87].

Unique spectral signatures. –

The ALTESSE Project. The identification of energetic materials has become a major issue in dual research, civil and military. A strong axis in this context concerns the acquisition of spectral signatures of explosives or hazardous materials upon large distances. The French project ALTESSE [88] (Air Laser-based TErahertz SpectroScopy of Explosives) aimed at testing the nonlinear terahertz spectroscopy from atmospheric plasmas. Dedicated scientific tasks consisted of (i) optimizing THz emission in a

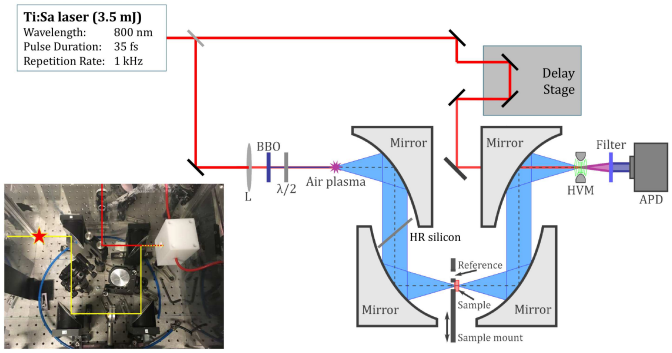

Fig. 4: Experimental device and ABCD detection system in transmission. SH (400 nm) is produced by a BBO crystal and focused with FH (800 nm) in the air by a lens (L). The THz radiation (blue stripes) from the plasma is filtered by a silicon wafer and collected by a set of off-axis parabolic mirrors. The delay line allows to probe the different instants of the THz pulse near the detection zone. The coupling between the focused probe beam and a high voltage module (HVM) creates a second harmonic in air detected by an avalanche photodiode (APD).

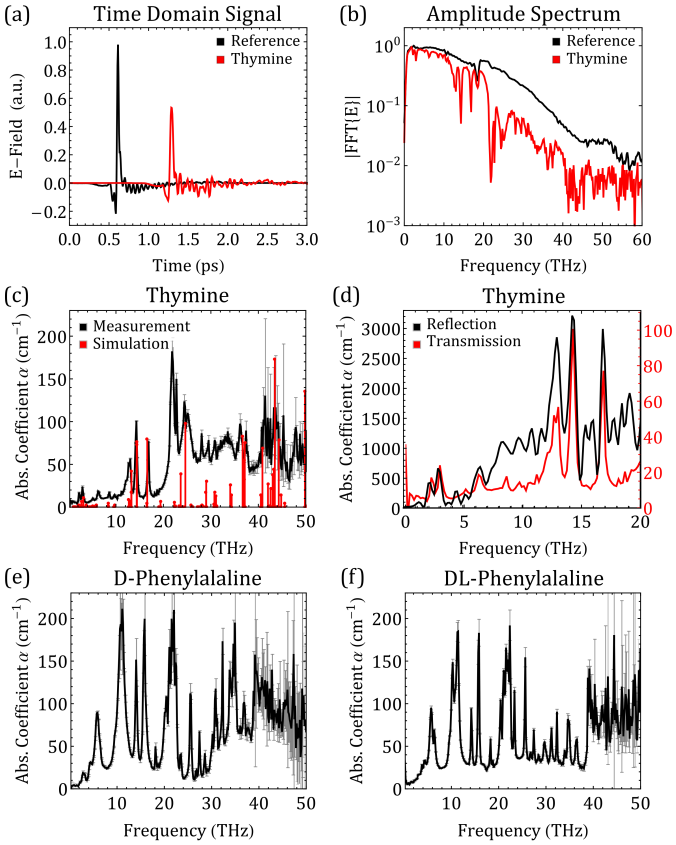

Fig. 5: (a) THz fields from the reference (nitrogen) and the sample (thymine pellet). (b) Transmission spectra obtained by Fourier transform. (c) Extracted absorption spectrum [$\alpha(\omega)$]. Red bars indicate the position and relative amplitude of CASTEP-calculated phonon modes. (d) Corresponding reflection spectrum. (e,f) show two transmission spectra of stereoisomers: (e) D-phenylalaline and (f) DL-phenylalaline. Thin vertical black lines indicate experimental error bars.

wide spectral window using two-color pulses; (ii) performing ABCD-based THz-TDS over distances larger than 10 m; (iii) carrying out spectroscopy in transmission and reflection geometries. Many materials have been analyzed in the THz-to-far-infrared domain and we here reveal unique signatures beyond 10 THz, using two-color air plasmas.

Broadband THz emitters. The ALTESSE facility operated at DTU/Fotonik [88] involved a generation part (800-nm laser line delivering 35-fs, 3.5 mJ pulses at 1 kHz repetition rate) and a detection part, as shown in fig. 4. After the BBO crystal, a half-wave plate rendered the FH polarization parallel to the SH. Both colors were focused into air and their relative phase was adjusted by the position of the doubling crystal. THz-TDS was carried out either in transmission or reflection. The samples were prepared in powders mixed with polyethylene, compressed into 1-mm-thick pellets and then mounted on a sample holder. The recorded temporal signals obtained with and without the sample were Fourier transformed to get their characteristic spectra. Figure 5(a) shows a reference THz field (black curve, without sample) and a THz field with the sample (red curve), which is thymine (nucleobasis). The reference signal is a single-cycle pulse having a duration of about 200 fs. The delay between both signals originates from the optical index of the sample. The spectrum transmitted by the latter shows many dips that correspond to its vibrational modes [see fig. 5(c)]. Here, we display the corresponding absorption coefficient $\alpha(\omega) = -(2/d)\ln[T^{-1}|E_{\text{sample}}(\omega)/E_{\text{reference}}(\omega)|]$, where d and T are the sample thickness and a transmission factor, respectively. The presence of features from 5 THz up to 60 THz demonstrates the rich potential of an ultra-broadband THz spectroscopy for the precise identification of complex molecules. We also performed THz spectroscopy in reflection geometry by inserting a golden mirror between the last two parabolic mirrors in the setup of fig. 4. The reflected THz spectrum shown in fig. 5(d) restores thymines's main peaks located within a 20-THz-broad spectral window. Figures 5(e,f) detail the preciseness supplied by this method to discriminate between stereoisomers of the same molecule. Here we observe the four characteristic peaks of the D- and DL-phenylalanine at the same position with similar amplitude. These spectra, however, exhibit differences at low frequencies, which demonstrates the ability of an ABCD-based broadband THz spectroscopy to distinguish different isomers.

Ab-initio numerical calculations. Computations based on the density functional theory were conducted using the code CASTEP (Cambridge Serial Total Energy Package [89]). CASTEP performs calculations of molecular crystal eigenmodes corresponding to the phonon frequencies (or energies) in a simulated unit cell (60 atoms/cell). These data enable us to compare the calculated phonon modes with the measured absorption spec-

tra, and also to visualize the molecular motions in the crystal. As an example, figs. 5(c) and 6(a,b) show the absorption spectrum of thymine and of two explosives, PETN and TATB, where their calculated phonon modes are plotted. Both positions and relative amplitudes of the latter are in reasonable agreement with the experimental lines. The four most important modes for thymine are 3.1 THz, 13.6 THz, 14.4 THz and 16.6 THz. At 3.1 THz, molecules in the unit cell rotate relative to each other, which corresponds to an intermolecular motion of the whole crystal. Going to higher frequencies, the crystal undergoes intramolecular vibrations. PETN owns six distinct peaks in the frequency range of 1 to 16 THz, above which the signal becomes noisy (see uncertainty bars). For TATB, the spectrum evidences characteristic signatures at 3.5 THz associated with intermolecular torsion, then at 8.5 and 13 THz associated with intramolecular angular oscillations.

Remote detection. To end with, figs. 6(c-e) show spectra collected with a terawatt (5 mJ, 40 fs) Ti:Sa laser operating at 100 Hz repetition rate, which was located at 15 meters from the ABCD detection system. The environment was bearing strong variations in temperature and presence of dust and vibrations. We met stability problems in the laser beam energy and directionality triggered by erratic temperature variations of $\pm 3°$ C, which led us to acquire spectra over short times ($<$ 10 min) and integration times of 100 ms (300 ms used at DTU). These spectra were reproduced 3 times for validation. Figure 6(c) displays the first-to-date 18-THz broad THz spectrum of PETN measured with remote laser source. The 800-nm pump pulse freely propagated a distance $>$ 10 m before reaching the optical table where the BBO crystal, the sample and ABCD setup were positioned. There, the two-color pulse was then focused by a 20-cm lens and created a plasma producing radiation directed to the detection zone. The red curve in fig. 6(c) shows the measured spectrum from a nitrogen-saturated detection chamber. Note the very good agreement with the PETN spectrum measured in clean laboratory conditions (black curve) without long-range pump pulse propagation. Figures 6(d,e) compare the THz spectra of TATB and ANTA (explosives) measured with the same remote laser source (ISL) and in clean atmosphere (DTU). The remote signals are less resolved due to the above limitations. However, they still contain the main spectral signatures of TATB and even achieve an excellent agreement for the ANTA. Hence, these results demonstrate that, even in noisy atmosphere and over large distances $>$ 10 m, a rapid acquisition of numerous spectral signatures, over a broad bandwidth covering about 20 THz, is feasible and robust.

Conclusion. – Terahertz pulses produced by ultrafast lasers are able to cover a wide range of frequencies, from gigahertz to mid-infrared, and offer rich perspectives for characterizing many materials. In this article, two-color plasma sources of terahertz radiation driven by photocurrents were discussed. Fully exploiting this nonlinear conversion mechanism, the ALTESSE project demonstrated the promising capabilities of portable laser devices for operating an effective, remote detection of suspect materials, including explosives.

* * *

The authors thank ANR and DGA for funding the ASTRID Project "ALTESSE" (ANR-15-ASTR-0009). They also acknowledge support from Laserlab.dk (Danish Center for Laser Infrastructure).

REFERENCES

[1] Tonouchi M., *Nat. Photon.*, **1** (2007) 9691.
[2] Chen J. *et al.*, *Opt. Express*, **15** (2007) 12060.
[3] Leahy-Hoppa M. R. *et al.*, *Chem. Phys. Lett.*, **434** (2007) 227.
[4] Frederici J. F. *et al.*, *Semicond. Sc. Techn.*, **20** (2005) S266.
[5] Kemp M. C. *et al.*, *Proc. SPIE*, **5070** (2003) 44.
[6] Shen Y. C. *et al.*, *Appl. Phys. Lett.*, **86** (2005) 241116.
[7] Fischer B. M. *et al.*, *Proc. IEEE*, **95** (2007) 1592.
[8] Pereira M. F. and Oleksiy Sh., *THz for CBRN and Explosives Detection and Diagnosis*, edited by Springer 2017
[9] Liu J. *et al.*, *J. Phys.: Conf. Series*, **680** (2016) 012030.
[10] Franz M. *et al.*, *J. Mol. Struct.*, **1006** (2011) 34.
[11] Berry E. *et al.*, *J. Laser Appl.*, **15** (2003) 192.
[12] Yu C. *et al.*, *Quant. Imaging Med. Surg.*, **2** (2012) 33.
[13] Gente R. and Koch M., *Plant Methods*, **11** (2015) 15.
[14] Hafez H. A. *et al.*, *J. Opt.*, **18** (2016) 093004.
[15] Klymenko M and Shulika Oleksiy V. and Sukhoivanov I. A., *Terahertz Spectroscopy - A Cutting Edge Technology*, edited by InTech 2017
[16] Crowe Th. *et al.*, *Proc. IEEE*, **80** (1992) 1827
[17] Maestrini A. *et al.*, *Comptes Rendus Physique*, **11** (2010) 480
[18] Kazarinov R., *Sov. Phys.-Semicond.*, **5** (1971) 707.
[19] Faist J. *et al.*, *Science*, **264** (1994) 553.
[20] Walther C. *et al.*, *Appl. Phys. Lett.*, **91** (2007) 131122.
[21] Bachmann D. *et al.*, *Optica*, **3** (2016) 1087.
[22] Auston D. H. *et al.*, *Phys. Rev. Lett.*, **53** (1984) 1555.
[23] Suen J. Y. *et al.*, *Appl. Phys. Lett.*, **96** (2010) 141103.
[24] Shen Y. C. *et al.*, *Appl. Phys. Lett.*, **83** (2003) 3117.
[25] Hale P. J. *et al.*, *Opt. Express*, **22** (2014) 26358.
[26] Yardimci N. T. *et al.*, *IEEE Trans. Terahertz Sci. Technol.*, **5** (2015) 223.
[27] Ropagnol X *et al.*, *Opt. Express*, **24** (2016) 11299.
[28] Boyd R. W., *Nonlinear Optics*, edited by Academic Press (San Diego) 2008
[29] Sun F. G. *et al.*, *CLEO 2000 Tech. Digest*, **39** (2000) 479.
[30] Blanchard F *et al.*, *Opt. Express*, **15** (2007) 13212.
[31] Loeffler T. *et al.*, *Opt. Express*, **13** (2005) 5353.
[32] Hebling J. *et al.*, *Appl. Phys. B*, **78** (2004) 593.
[33] Hebling J. *et al.*, *Opt. Express*, **10** (2002) 1161.
[34] Blanchard F. *et al.*, *Opt. Lett.*, **39** (2014) 4333.
[35] Huang S. W. *et al.*, *Opt. Lett.*, **38** (2013) 796.
[36] Vicario C. *et al.*, *Phys. Rev. Lett.*, **112** (2014) 213901.
[37] Löffler T. and Jacob F. and Roskos H. G., *Appl. Phys. Lett.*, **77** (2000) 453.

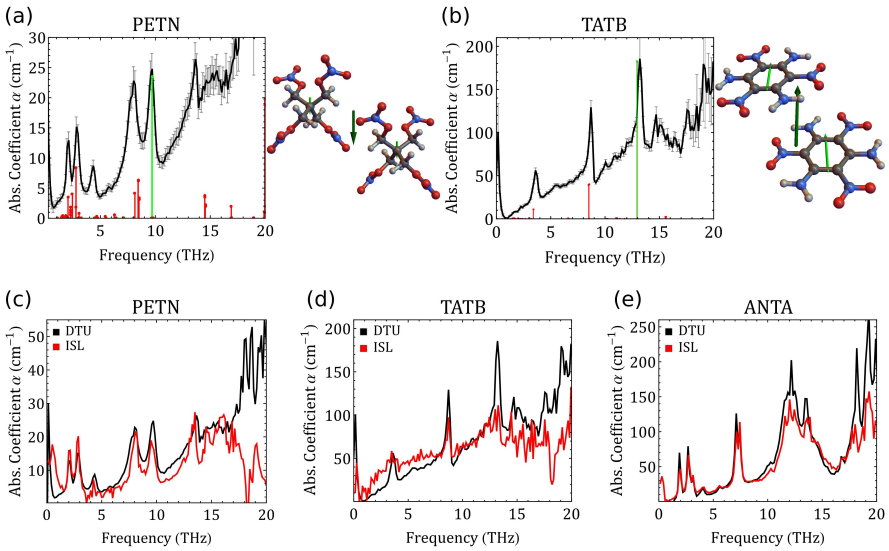

Fig. 6: Absorption spectra (black curves) and simulated phonon modes (red bars) for (a) PETN and (b) TATB. Thin vertical black lines correspond to experimental error bars. On the right, characteristic molecular structures illustrating dipole excitations are shown (red: O, blue: N, grey: H atoms). Arrows indicate the center of mass dipole moments: the big arrow at center shows the total dipole moment of the unit cell related to the green absorption line; the two smaller arrows in the center of each molecule are the respective net dipole moments. (c-e) Absorption spectra collected in transmission far from the laser output for (c) PETN, (d) TATB and (e) ANTA. Red curves are spectra measured at Institut Saint-Louis (ISL - France) with the Ti:Sa source located at a distance of 15 m from the ABCD system. Black curves are spectra measured in the laboratory over optical propagation paths of less than 1 m in clean atmosphere (DTU/Fotonik - Denmark).

[38] Cook D. J. and Hochstrasser R. M., *Opt. Lett.*, **25** (2000) 1210.
[39] Kress M. *et al.*, *Opt. Lett.*, **29** (2004) 1120.
[40] Kim K. Y. *et al.*, *Nat. Photon.*, **2** (2008) 605.
[41] Kim K. Y. *et al.*, *Opt. Express*, **15** (2007) 4577.
[42] Braun A *et al.*, *Opt. Lett.*, **20** (1995) 73
[43] Bergé L. *et al.*, *Rep. Prog. Phys.*, **70** (2007) 1633.
[44] Bergé L. *et al.*, *Phys. Rev. Lett.*, **110** (2013) 073901.
[45] D'Amico C. *et al.*, *Phys. Rev. Lett.*, **98** (2007) 235002.
[46] Daigle J.-F. *et al.*, *Opt. Express*, **20** (2012) 6825.
[47] Clerici M. *et al.*, *Phys. Rev. Lett.*, **110** (2013) 253901.
[48] Wang T.-J. *et al.*, *Appl. Phys. Lett.*, **97** (2010) 111108.
[49] González de Alaiza Martínez P. *et al.*, *Phys. Rev. Lett.*, **114** (2015) 183901.
[50] Hamster H. *et al.*, *Phys. Rev. Lett.*, **71** (1993) 2725.
[51] Gopal A. *et al.*, *Opt. Lett.*, **38** (2013) 4705.
[52] Liao G. Q. *et al.*, *Phys. Rev. Lett.*, **114** (2015) 255001.
[53] Gopal A. *et al.*, *Phys. Rev. Lett.*, **111** (2013) 074802.
[54] Leemans W. P. *et al.*, *Phys. Rev. Lett.*, **91** (2003) 074802.
[55] Liao G. Q. *et al.*, *Phys. Rev. Lett.*, **116** (2016) 205003.
[56] Déchard J. *et al.*, *Phys. Rev. Lett.*, **120** (2018) 144801.
[57] Herzer S. *et al.*, *New J. Phys.*, **20** (2018) 063019.
[58] Zhang X. C. *et al.*, *Nat. Photon.*, **11** (16) 2017.
[59] Wu Q. and Zhang X.-C., *Appl. Phys. Lett.*, **70** (1997) 1784.
[60] Leitenstorfer A. *et al.*, *Appl. Phys. Lett.*, **74** (1999) 1516.
[61] Sharma G. *et al.*, *Opt. Lett.*, **37** (2012) 4338.
[62] Xie X. *et al.*, *Phys. Rev. Lett.*, **96** (2006) 075005.
[63] Dai J.-M. *et al.*, *Phys. Rev. Lett.*, **97** (2006) 103903.
[64] Karpowicz N. *et al.*, *Appl. Phys. Lett.*, **92** (2008) 011131.
[65] Liu K. and Zhang X.-C., *THz for CBRN and Explosives Detection and Diagnosis*, edited by Springer (Dordrecht, Netherlands) 2017
[66] Klarskov P. *et al.*, *New J. Phys.*, **15** (2013) 075012.
[67] Sharma G. *et al.*, *Opt Lett.*, **38** (2013) 2705.
[68] Liu J. and Zhang X.-C., *Phys. Rev. Lett*, **103** (2009) 235002.
[69] Liu J. *et al.*, *Nat. Photon.*, **4** (2010) 627.
[70] Dai J. *et al.*, *IEEE J. Sel. Top. Quantum*, **17** (2011) 183.
[71] Tomasino A. *et al.*, *Optica*, **4** (2017) 1358.
[72] Andreeva V. A. *et al.*, *Phys. Rev. Lett.*, **116** (2016) 063902.
[73] Babushkin I. *et al.*, *New J. Phys.*, **13** (2011) 123029.
[74] Nguyen A. *et al.*, *Opt. Express*, **25** (2017) 4720.
[75] Keldysh L. V., *Sov. Phys. JETP*, **20** (1965) 1307.
[76] Perelomov A. M. *et al.*, *Sov. Phys. JETP*, **23** (1966) 924.
[77] Thomson M. D. *et al.*, *Laser Photon. Rev.*, **1** (2007) 349.
[78] Babushkin I. *et al.*, *Phys. Rev. Lett.*, **105** (2010) 053903.
[79] Debayle A. *et al.*, *Opt. Express*, **22** (2014) 13691.
[80] Zhang L.-L. *et al.*, *Phys. Rev. Lett.*, **119** (2017) 235001.
[81] You Y. S., *Phys. Rev. Lett*, **109** (2012) 183902.
[82] D'Amico C. *et al.*, *New J. Phys.*, **10** (2007) 013015.
[83] Sprangle P. *et al.*, *Phys. Rev. E*, **69** (2004) 066415.
[84] Thiele I. *et al.*, *Phys. Rev. E*, **94** (2016) 063202.
[85] Miao Ch. *et al.*, *Phys. Plasmas*, **20** (2018) 063019.
[86] González de Alaiza Martínez P. *et al.*, *Scient. Reports*, **6** (2016) 26743.
[87] Thiele I. *et al.*, *Optica*, **5** (2018) 1617.
[88] ALTESSE Website: www.agencenationale-recherche.fr/Project-ANR-15-ASTR-0009,.
[89] Clark S. J. *et al.*, *Zeit. Kristal.*, **220** (2005) 567.